Joint P-P and P-S seismic inversion

Gary F. Margrave and Robert R. Stewart, CREWES, University of Calgary
Jeffrey A. Larsen, Husky Energy, Calgary

INTRODUCTION

We present a case history of joint inversion of P-P and P-S reflection seismic data using a weighted stacking technique. Our example comes from the Blackfoot field, owned and operated by PanCanadian Petroleum Ltd., in southeastern Alberta, Canada. The exploration target at Blackfoot is a Lower Cretaceous channel system at approximately 1.4 km depth (Figure 1). These Glauconitic channels, with sand or shale fill, are found throughout the region, and, as there were many episodes of channel formation, can be stacked on top of one another. At Blackfoot, the channel interval is about 40 m thick and 100 m wide. There tends to be good porosity in an *upper channel* and a *lower channel* that are separated by a tight, *lithic channel*. The *upper channel*, where present, is usually gas-prone, while the *lower channel* is generally oil-prone. When the pore fluid in the channel sands is a compressible hydrocarbon instead of incompressible water, the bulk compressibility is reduced and this modifies the signature of seismic reflection data. Since pressure waves and shear waves sense different rock and pore-fluid properties, joint use of P-P and P-S data can provide superior lithologic discrimination.

This article proceeds with a theoretical examination the nature of P-P and P-S reflections with examples specific to Blackfoot. It continues with a description of the algorithm for least-squares inversion of either P-P seismic alone or the joint inversion of P-P and P-S data. Then we present our specific methodology for the practical implementation of these inversions. The final section presents the results of both inversions, P-P data alone and joint P-P and P-S data, applied to the Blackfoot data.

UNDERSTANDING P-P AND P-S REFLECTIONS

The conversion of one elastic wave, either P or S, into another upon reflection or transmission at an interface is described by the *Zoeppritz equations*. The complete Zoeppritz equations are most conveniently found in the classic text by Aki and Richards (1980) (see *Suggestions for further reading* at the end of this article) while an excellent historical and practical discussion is given by Castagna (1993). These equations are algebraically quite complex and it is not practical to reproduce them here. (We invite the reader to visit our website, www.crewes.org, and

interactively examine the equations using our *Zoeppritz explorer*.) Instead, we will present useful concepts and approximate forms. Since there are four possible incident waves, upcoming and downcoming P and S, and four possible scattered waves, upgoing and downgoing P and S, there are sixteen scattering coefficients that link them. For example, the ratio of the magnitude of the particle displacement of the reflected P wave to that of the incident P wave gives the *P-P reflection coefficient* that we will call R_{pp}. Actually, there are two possible R_{pp}'s, corresponding either to incidence from above or from below, and they are generally different. In the case of a wave traveling straight down and incident upon a horizontal interface, called *normal incidence*, R_{pp} takes the familiar form $R_{ppN} = (I_2 - I_1)/(I_2 + I_1)$ where I_1 indicates the P-wave impedance of the medium containing the incident wave and I_2 is the impedance of the medium of the transmitted wave. For incidence from below, simply switch the layer subscripts in this formula to see that R_{ppN} for incidence from below is the negative of that for incidence from above. (This is only strictly true for normal incidence.)

The normal incidence R_{pp} can be written in other suggestive ways. If we define the *impedance contrast*, $\Delta I = I_2 - I_1$, and the *average impedance*, $I = (I_2 + I_1)/2$, then $R_{ppN} = .5\,\Delta I/I$. Going further, since P-wave impedance is the product of density, ρ, and P-wave velocity, α, it turns out that $R_{ppN} = .5(\Delta\alpha/\alpha + \Delta\rho/\rho)$. The ratios in the parenthesis are called the *P-wave velocity fluctuation*[1], $f_\alpha = \Delta\alpha/\alpha$, and the *density fluctuation*, $f_\rho = \Delta\rho/\rho$, so that $R_{ppN} = .5 f_\alpha + .5 f_\rho$. This suggests the very useful *Aki and Richards approximation* that $R_{pp} \approx c_\alpha f_\alpha + c_\rho f_\rho + c_\beta f_\beta$. Here f_β is the *S-wave velocity fluctuation* and the coefficients $c_\alpha, c_\rho, c_\beta$ depend upon the P-wave and S-wave incidence and reflection angles and the average α, β, ρ but not upon $\Delta\alpha, \Delta\beta, \Delta\rho$.

Comparing the normal incidence form of R_{pp} to the Aki and Richards approximation shows that, for an incidence angle of 0°, $c_\alpha = c_\rho = .5$ and $c_\beta = 0$. So at normal incidence, R_{pp} carries information about f_α and f_ρ in equal amounts and nothing at all about f_β. This situation

---

[1] These are actually *fractional fluctuations* not absolute fluctuations though we prefer the simple term *fluctuation*.

changes as we move to nonzero offset and $c_\alpha, c_\rho, c_\beta$ depart from their normal values of $(.5,.5,0)$. If we let θ denote the average of the P-wave angles of incidence and transmission and φ be the average of the S-wave angles of reflection and transmission, then the variation of $c_\alpha, c_\rho, c_\beta$ with offset can be represented either as dependence on θ or upon φ since these angles are related by Snell's law. Also c_ρ, c_β are not independent of one another in fact $c_\rho = .5 + .5c_\beta$. Precisely how these coefficients vary depends upon the specific values of the elastic constants so we will analyze the two cases shown in Table 1. These cases are idealized examples of the regional and reservoir behavior, at the stratigraphic level of the top of the channel, in the Blackfoot field. In both reservoir and regional settings, the fluctuations $f_\alpha, f_\rho, f_\beta$ have the same sign with α and ρ decreasing while β increases. However, the magnitude of these changes is much great in the reservoir case. The reservoir values in this table correspond to the blocked oil-well logs shown in Figure 2, that give values of α, β, ρ throughout the channel interval. Regional logs are not shown here.

Lithology	P-wave velocity (m/s)			S-wave velocity (m/s)			Density (gm/cc)		
	Upper	Lower	f_α	Upper	Lower	f_β	Upper	Lower	f_ρ
Regional	4100	4000	-0.025	2180	2200	0.009	2.5	2.45	-0.02
Reservoir	4100	3800	-0.076	2180	2350	0.075	2.5	2.4	-0.041

Table 1. Elastic properties for idealized *regional* and *reservoir* lithologies. In each case, two sets of elastic properties are given corresponding to above and below an interface.

Figure 3 shows the behavior of $c_\alpha, c_\rho, c_\beta$ for both the reservoir and non-reservoir cases. As incidence angle increases, c_α increases rapidly and nonlinearly. On the other hand, c_ρ, c_β trend in the opposite direction and seem almost parallel. This is precisely the behavior expected from the relation $c_\rho = .5 + .5c_\beta$. There are only subtle differences between these curves for the regional and reservoir lithologies.

Figure 4 shows what happens when the curves $c_\alpha, c_\rho, c_\beta$ are scaled by the fluctuations $f_\alpha, f_\rho, f_\beta$. Now there is a dramatic distinction between the regional setting and the reservoir. In

the regional case, the total R_{pp} is completely dominated by the P-wave velocity term, $c_\alpha f_\alpha$ and shows an overall negative reflection coefficient that increases slightly with angle. However, for the reservoir, both f_α and f_β are much larger and the total R_{pp} now has a significant contribution from $c_\beta f_\beta$ that becomes more important with increasing angle. The density term $c_\rho f_\rho$ has only a slight effect near normal incidence. The total R_{pp} for the reservoir has a strong negative response at normal incidence that becomes increasingly more negative with angle.

Aki and Richards also provide an approximate form for the reflection coefficient for a P-wave converting to and S-wave as $R_{ps} \approx d_\beta f_\beta + d_\rho f_\rho$. As before, the coefficients d_β, d_ρ depend upon either the P-wave angle θ or the S-wave angle φ and the average (background) elastic parameters. As with the P-wave case, the density and S-wave coefficients are not completely independent though the relation between them is more complicated: $d_\rho = -\sin\theta / (2\cos\varphi) + .5d_\beta$. Using the values from Table 1, Figure 5 shows the behavior of d_β, d_ρ versus P-wave incidence angle and, again, the curves change very little from the regional to the reservoir scenario. However, as shown in Figure 6, when these curves are scaled by the relevant fluctuations and combined, the reservoir becomes quite distinct from regional behavior. Interestingly, at the top of the upper channel, as the density and S-wave fluctuations have opposite signs a small R_{ps} of about -.01 absolute maximum results. At the angle of this maximum, R_{pp} is about -.1 (Figure 4).

At the base of the channel the density and S-wave fluctuations are of the same sign (Figure 2), while similar in magnitude to those at the reservoir top, so their partial reflectivities reinforce resulting in a much stronger response. More precisely, from Figure 2 we can conclude that $f_\beta \sim .083$ and $f_\rho \sim .041$ and the resulting R_{ps} is given by the green-dotted curve in Figure 6. The absolute maximum of this curve is near -.06 and suggests that P-S reflections can be as strong as P-P. We routinely observe this to be the case.

We close this section with the synthetic P-P and P-S reflection seismograms shown in Figure 7. There are many possible methods for building synthetic elastic seismograms but often such techniques are computationally intensive and produce overly complex wavefields. If the seismograms are to be compared to processed data, then we often ignore many complexities,

such as attenuation and multiples because data processing is designed to attenuate them. Our method, described by Lawton and Howell (1992, SEG Expanded Abstracts), uses raytracing to determine traveltimes and the exact Zoeppritz equations to calculate the primary reflectivity. The elastic parameters at each depth were obtained from the same dipole sonic and density logs that are shown blocked in Figure 2. This method has the advantages of being rapid and simple while still producing realistic seismograms. The synthetic seismograms shown here have primaries only (no multiples), no transmission losses or spherical spreading losses, and have normal moveout removed; but moveout stretch effects are present. Both seismograms were created initially as broadband responses and then convolved with appropriate wavelets. The P-P seismogram has a 10-80 Hz, zero-phase, wavelet installed while the P-S seismogram has a 10-40 Hz wavelet. These choices model the recovered bandwidths of the Blackfoot data. It is our common experience that P-S data recorded on land has about half the bandwidth of the corresponding P-P data. Nevertheless, as these seismograms show, their resolving power is similar. Roughly speaking, this is a consequence of S-wave wavelengths being about half of the P-wave since the typical velocity ratio is $\alpha/\beta = 2$. These seismograms are displayed such that a net impedance increase appears as a positive amplitude on both plots.

LEAST-SQUARES INVERSION

P-P inversion

The idea of least-squares inversion of P-P data is usually credited to Smith and Gidlow (1987) who showed that the Aki and Richards approximation for R_{pp} can be inverted by least squares to estimate the fluctuations $f_\alpha, f_\beta, f_\rho$. In their method, P-P reflection data are assumed to provide estimates of R_{pp} over a range of source-receiver offsets. Thus, for each offset, x, an equation can be written like

$$R_{pp}\left(x(\theta)\right) = c_\alpha(\theta) f_\alpha + c_\rho(\theta) f_\rho + c_\beta(\theta) f_\beta$$

where we note the explicit dependence on the incidence angle, θ. Then, considering all available offsets, a matrix equation can be constructed

$$\begin{bmatrix} R_{pp}(x_1) \\ R_{pp}(x_2) \\ \vdots \\ R_{pp}(x_n) \end{bmatrix} = \begin{bmatrix} c_\alpha(\theta_1) & c_\rho(\theta_1) & c_\beta(\theta_1) \\ c_\alpha(\theta_2) & c_\rho(\theta_2) & c_\beta(\theta_2) \\ \vdots & \vdots & \vdots \\ c_\alpha(\theta_n) & c_\rho(\theta_n) & c_\beta(\theta_n) \end{bmatrix} \begin{bmatrix} f_\alpha \\ f_\rho \\ f_\beta \end{bmatrix}.$$

The left side of this equation is a column vector representing the amplitudes of a particular P-P reflection as a function of offset. The $(n \times 3)$ matrix on the right contains the coefficients $c_\alpha, c_\rho, c_\beta$ computed at the appropriate incidence angle for each offset. This matrix is approximately known if a *background* velocity model is available to raytrace through to obtain the incidence angles. Finally, the column vector on the right contains the unknown fluctuations to be estimated. If there are more than three offsets, there are more equations than unknowns and least-squares inversion is appropriate. Writing this equation symbolically as $\underline{R} = \underline{\underline{C}}\,\underline{f}$, its least-squares inverse is $\underline{f} = \underline{\underline{A}}\,\underline{R}$ where $\underline{\underline{A}} = \left(\underline{\underline{C}}^T \underline{\underline{C}}\right)^{-1} \underline{\underline{C}}^T$. Smith and Gidlow were able to calculate the entries in the matrix $\underline{\underline{A}}$ analytically and showed that the algorithm $\underline{f} = \underline{\underline{A}}\,\underline{R}$ is just a weighted stack. That is, f_α can be estimated, in principle, by an equation of the form

$$f_\alpha = \sum_{k(offset)} a(\theta_k) R_{pp}(\theta_k)$$

with similar equations, having different weighting functions, for f_β, f_ρ. In this equation, the sum is over all available offsets and the weights, $a(\theta_k)$, are known functions of the background velocity and the incidence angle for the kth offset. Usually, it is expected that the overall density effect on R_{pp} is small and this implies that inversion for f_ρ will be problematic with noisy data. Smith and Gidlow suggested using Gardner's relation that $\rho \sim k\alpha^{.25}$ (k is a constant whose numerical value depends upon the system of units employed) to convert the density dependence into an additional P-wave velocity term. An alternative approach is the approach of Fatti et al. (1994) who reformulated the equations to invert for fluctuations associated with P-wave and S-wave impedances: $f_I = \Delta(\rho\alpha)/(\rho\alpha)$ and $f_J = \Delta(\rho\beta)/(\rho\beta)$. This avoids the use of Gardner's rule but there is still an independent f_ρ term that must be neglected. Fortunately, the coefficient of this term is generally small.

Given estimates of the fluctuations, either f_α, f_β or f_I, f_J, other lithologic indicators can be formed. Among these are the *pseudo Poisson's ratio fluctuation*, $f_\alpha - f_\beta$ (also called the fluctuation in the P-wave to S-wave velocity ratio $r = \alpha/\beta$), the Smith-Gidlow *fluid factor*, $f_\alpha - 1.16 f_\beta r$, and the fractional Lame parameters (Goodway et al. 1997). All of these have value in discriminating lithologies.

P-P and P-S joint inversion

Stewart (1990) derived the extension of the Smith-Gidlow approach that uses both P-P and P-S reflections to constrain the fluctuations $f_\alpha, f_\beta, f_\rho$. Larsen et al. (1998) and Larsen (1999) presented a practical implementation of these ideas as applied to the Blackfoot 3C-3D survey. Like Smith and Gidlow, Stewart developed exact analytic forms for the stacking weights of both P-P and P-S data. The algebraic expressions for these weights are too complex to present in this paper. However, we invite the interested reader to download Larsen's thesis from www.crewes.org for a complete description. In essence, the fluctuations are estimated by equations of the form

$$f_\alpha = \sum_{k(offset)} a(\theta_k) R_{pp}(\theta_k) + \sum_{k(offset)} b(\theta_k) R_{ps}(\theta_k)$$

where θ_k is the P-wave incidence angle for the kth offset, $a(\theta_k)$ are the stacking weights for the P-P reflection data, and $b(\theta_k)$ are the weights for the P-S reflection data. Similar equations, with different weights, will estimate f_β or f_ρ. The weights for the P-P reflection data, $a(\theta_k)$, in this expression are generally quite different from the analogous weights in the inversion using P-P data alone.

As with the P-P case, it is often preferable to bypass the estimation of f_ρ. Larsen (1999) shows that either the Smith-Gidlow approach using Gardner's rule or the Fatti approach of estimating impedance fluctuations is possible. In the latter case, there is again an f_ρ term that must be neglected. Interestingly, the possibility of a true three-parameter inversion for $f_\alpha, f_\beta, f_\rho$ is much more feasible with P-P and P-S data, though we do not discuss that here.

PRACTICAL IMPLEMENTATION

There are a number of practical difficulties that must be overcome to apply the joint inversion technique. Perhaps the most fundamental is the need to ensure that the P-P and P-S reflections that are stacked together come from the same reflection point in the earth. This implies two considerations: migration of both datasets and event-correlation between them. In a perfect world, both objectives would be met by a prestack depth migration of the P-P and P-S data volumes using the correct P and S velocities. This would collapse the Fresnel zones in both volumes and also establish event correlations automatically by whatever P-P and P-S energy becomes focused at each subsurface point. However, this is computationally intensive and requires software not commonly available, so we implemented a more practical approach using fairly standard technologies.

First, we developed conventional P-P and P-S data processing flows (from edit to stack) using established methods. For P-P data, this included amplitude recovery, deconvolution, statics adjustment, velocity analysis and NMO removal, and residual statics. For the P-S data, the flow was similar except that care was taken to ensure that the source statics were taken from the P-P data. Then the P-P data was stacked at the CMP (common mid-point) and the P-S data was stacked at the CCP (common conversion point). In this way, final stacks were created that were appropriate for post-stack migration. However, to retain information about the variation of reflectivity with offset, each dataset was segmented into five limited-offset stacks as shown in Figure 8. The offset ranges were chosen by determining the maximum offset available at the target reflection and dividing it into equal intervals. The choice of five offset ranges was determined only by a desire to limit the required work. More offset bins would result in less averaging and, perhaps, superior resolution.

After stack, the ten 3D data volumes were taken through an event enhancement process of time-variant spectral whitening (TVSW), spatial prediction (f-x-y), and then into P-P or P-S post-stack time-migration (Figure 9). The flattening step in the center of Figure 9 was preceded by event correlation to establish identity of key reflection events.

Event correlation was accomplished by building synthetic P-P and P-S seismograms (Figure 7) and tying them to the migrated reflection data. The seismograms were generated over the same range of offsets as the reflection data and stacked into the same offset bins. Following

event correlation, the five P-P and five P-S volumes were flattened on a reference event just above the channel and converted to depth relative to this event.

The amplitude restoration box of Figure 9 refers to a process designed to restore the average AVO behavior of both P-P and P-S data volumes. Our processing included trace-to-trace amplitude balancing (trace equalization) prior to formation of the limited offset stacks. This was deemed necessary as an aid to stacking-out undesirable noise; however, it does equalize the energy of traces across offset. As we have seen, P-S reflection strength should vanish at zero offset and vary roughly as $\sin\theta$ with increasing offset. On the other hand P-P reflection strength is significant at zero offset and may either increase or decrease with offset. This behavior was imposed upon our data by using the elastic synthetic seismograms (Figure 7) mentioned above as a guide. For each offset, the rms (root-mean-square) amplitude of each trace of the reflection data was adjusted to match that of the corresponding elastic synthetic seismogram. For example, each trace of the P-S data binned over offsets from 1050 to 1750 m was matched in rms amplitude to the P-S synthetic seismogram response representing the stacked P-S response over these offsets.

At this stage, the five P-P and five P-S 3D volumes can be considered as bandlimited estimates of R_{pp} and R_{ps}. Since they were converted to depth relative to the top of the channel, horizon slices taken from these volumes just beneath the reference depth should correspond to the same stratigraphic level. The weighted stacking scheme was then implemented by weighting and summing these horizon slices at each desired depth (Figure 10). In particular, estimates of $f_I = \Delta(\rho\alpha)/(\rho\alpha)$ and $f_J = \Delta(\rho\beta)/(\rho\beta)$ were produced. The pseudo-Poisson's ratio fluctuation was also estimated as $f_I - f_J$.

RESULTS

Figure 11 shows the result of a simple series of experiments on synthetic data from a single interface. The full Zoeppritz equations were used to generate exact R_{pp} and R_{ps}. In a noise-free case, both P-P inversion and joint P-P and P-S inversion produce identical estimates of the fluctuations. However, when random noise was added to the R_{pp} and R_{ps} values, the joint method becomes clearly superior. The simplest reason for this is that both methods constrain the same number of unknowns but the joint method uses twice as much data. This is much greater

statistical leverage. As this figure shows, the f_J estimates are most dramatically improved in the joint inversion and that leads to better estimates of the pseudo-Poisson's ratio fluctuation $f_I - f_J$.

Figures 12 and 13 show the weights computed for the estimation of $f_I = \Delta(\rho\alpha)/(\rho\alpha)$ and $f_J = \Delta(\rho\beta)/(\rho\beta)$ by the P-P method of Smith and Gidlow and the P-P & P-S joint method. The computation of these weights requires a background velocity model for both P- and S-wave propagation. This was obtained by strongly smoothing velocities from one of the dipole sonic logs at Blackfoot. For the shallow, unlogged section, a homogeneous layer was included that gave the observed total traveltimes. Examination of these weights shows that for both f_I and f_J estimates, the P-P method tends to subtract the far from the near offsets. This is a consequence of the Aki and Richards approximation that R_{pp} is a linear combination of $f_\alpha, f_\beta, f_\rho$. The joint method does some differencing of R_{pp} at shallow depths but tends towards a differencing of R_{pp} from R_{ps} at depth. The depth to the channel system (Figure 2) is at the very bottom of these figures.

Figure 14 shows the estimation of f_I at the stratigraphic level of the top of the upper channel. The vertical trend of the producing oil wells in the lower center of each image defines the proven channel location. The joint method indicates a larger and sharper anomaly associated with the production than the P-P method. Whether this anomaly is due to a production effect or, might it be present in a virgin setting, is the subject of other work. Figure 15 shows the corresponding estimation of f_J for the top of the channel. The P-P map estimates are dominantly > -.02 while the joint estimate has large regions that have $f_J < -.02$. The anomaly associated with the channel is similar on both maps. The areas of large negative f_J indicate low rigidity and are interpretable as shale. The joint-method inversion suggests a relatively rigid sand channel in regional shale that is consistent with the Blackfoot model shown in Figure 1. Figure 16 shows the estimate of pseudo-Poisson's ratio, $f_I - f_J$, that is simply the subtraction of the maps of Figure 15 from those of Figure 14. Interestingly, the anomaly associated with the producing wells is now much more consistent between the two techniques than for either of the previous

two Figures. However, the association of producing wells with low values of $f_I - f_J$ is more consistent for the joint inversion, especially for the wells 01-08 (bottom center) and 13-16 (upper right). Well 05-16 appears anomalous on both $f_I - f_J$ images.

These results suggest that the joint method give superior results compared to the P-P method for both f_I and f_J but that the estimation of $f_I - f_J$ is only marginally better. Put another way, the P-P method is directly sensitive to changes in Poisson's ratio but is less effective in estimating f_I and f_J individually. From the introductory exploration of the Zoeppritz equations, the P-P method must estimate and subtract f_J (equivalently f_β and f_ρ) from R_{pp} in order to estimate f_I. This process is strongly impeded by noise because f_J tends to be a small fraction of f_I. However, errors in the estimation of f_J tend to cause compensating errors in f_I such that the difference $f_I - f_J$ is relatively stable. The joint method measures f_J more directly and this better estimate allows a better estimate of f_I as well.

Figure 17 shows the f_I estimates for the base of the lower channel. A lineation associated the trend of producing wells is clearly evident on the joint inversion and largely absent from the P-P inversion. Precisely why this lineation should be numerically near zero is perplexing though we note that the channel thicknesses are generally below the dominant wavelength on both P-P and P-S data so that we are seeing tuned responses. Figure 18 shows the f_J response while Figure 19 displays the estimate $f_I - f_J$. In Figure 19 both methods associate a lineation with the channel though with different numerical values.

Property	RMS error compared to wells		$\dfrac{\sigma_{PP}}{\sigma_{PP+PS}}$
	$\sigma_{PP} = \text{P-P error}$	$\sigma_{PP+PS} = \text{P-P}$ & P-S error	
$f_I = \Delta(\rho\alpha)/(\rho\alpha)$	0.0238	0.0081	2.94
$f_J = \Delta(\rho\beta)/(\rho\beta)$	0.0215	0.0025	8.60

$f_I - f_J$	0.0316	0.0064	4.94

Table 2. The result of a statistical comparison of the P-P and simultaneous P-P and P-S inversions with well control. Seven wells were used, three had dipole sonics and density logs that give detailed information for α, β, ρ. The other four had acoustic sonics and density logs without shear-wave information.

Though the results from the joint inversion appear more interpretable, a more unambiguous assessment of the inversion results is desirable. Accordingly, we compared the estimated values of the fluctuations $f_I, f_J, f_I - f_J$ to well control. We used well logs taken at seven different wells including producers and dry holes. All wells had density logs and at least an acoustic sonic log, but importantly, three wells had dipole sonics that give both P-wave and S-wave velocities. Thus, we were able to compare the P-wave impedances at seven wells and the S-wave impedances at three wells. Values for the fluctuations, $f_I, f_J, f_I - f_J$, were calculated in the wells at a desired depth by averaging above and below the depth over about a wavelength and forming the difference of these local averages divided by their mean. Assuming the well information to be without error, Table 2 shows the errors, or standard deviations, for each fluctuation as estimated by each inversion technique. The Table also shows the ratio of the error from the P-P inversion divided by the error from the joint inversion. By this comparison, the P-wave impedance fluctuation, f_I, is estimated with 300% improvement using joint inversion while the S-wave impedance fluctuation, f_J, is nearly 900% better. Though it would be nice to have more well control to contribute more points to this statistical analysis, we are satisfied that it confirms the added advantage of the P-P and P-S joint inversion technique.

CONCLUSIONS

We have presented a practical method for the joint inversion of P-P and P-S reflection data and documented its performance, in comparison with P-P data alone, using the 3C-3D survey at Blackfoot field. Like the P-P method, the joint method is implemented as a weighted stack but with different weights and twice the statistical leverage. The joint method gives markedly superior estimates of the P-wave and S-wave impedance fluctuations, f_I and f_J, but only moderately better estimates of the pseudo-Poisson's ratio, $f_I - f_J$. We compared the inversion

results to well control and found a strong statistical edge for the joint method that supports our conclusions.

Suggestions for further reading.

Aki, K, and Richards, P. G., 1980, Quantitative Seismology Theory and Methods: W. H. Freeman and Co.

Castagna, J. P., 1993, AVO analysis – tutorial and review: in *Offset-dependent reflectivity – theory and practice of AVO analysis,* Investigations in Geophysics No. 8, Castagna, J. P. and Backus, M. P. (eds.), Society of Exploration Geophysicists, 3-36.

Fatti, J. L., Smith, G. C., Vail, P. J., Strauss, P. J., and Levitt, P. R., 1994, Detection of gas in sandstone reservoirs using AVO analysis: Geophysics, 59, 1362-1376.

Goodway, B., Chen, T., and Downton, J., 1997, Improved AVO fluid detection and lithology discrimination using Lame petrophysical parameters: "$\lambda\rho$", "$\mu\rho$", and "$\lambda\mu$ fluid stack", from P and S inversions: CSEG Expanded Abstracts, 148-151.

Larsen, J. A., Margrave, G. F., Lu, H, and Potter, C. C., 1998, Simultaneous P-P and P-S inversion by weighted stacking applied to the Blackfoot 3C-3D survey: CREWES Research Report, vol. 10. (Available at www.crewes.org)

Larsen, J. A., 1999, AVO inversion by simultaneous P-P and P-S inversion: M.Sc. thesis, The University of Calgary. (Available at www.crewes.org)

Lawton, D. C., and Howell, T. C., 1992, P-P and P-SV synthetic stacks: Expanded Abstracts, 62nd SEG, 1344-1347.

Smith, G. C., and Gidlow, P. M., 1987, Weighted stacking for rock property estimation and detection of gas: Geophys. Prosp., 35, 993-1014.

Stewart, R. R., 1990, Joint P and P-SV inversion: CREWES Research Report, vol. 3., (Available at www.crewes.org).

FIGURES
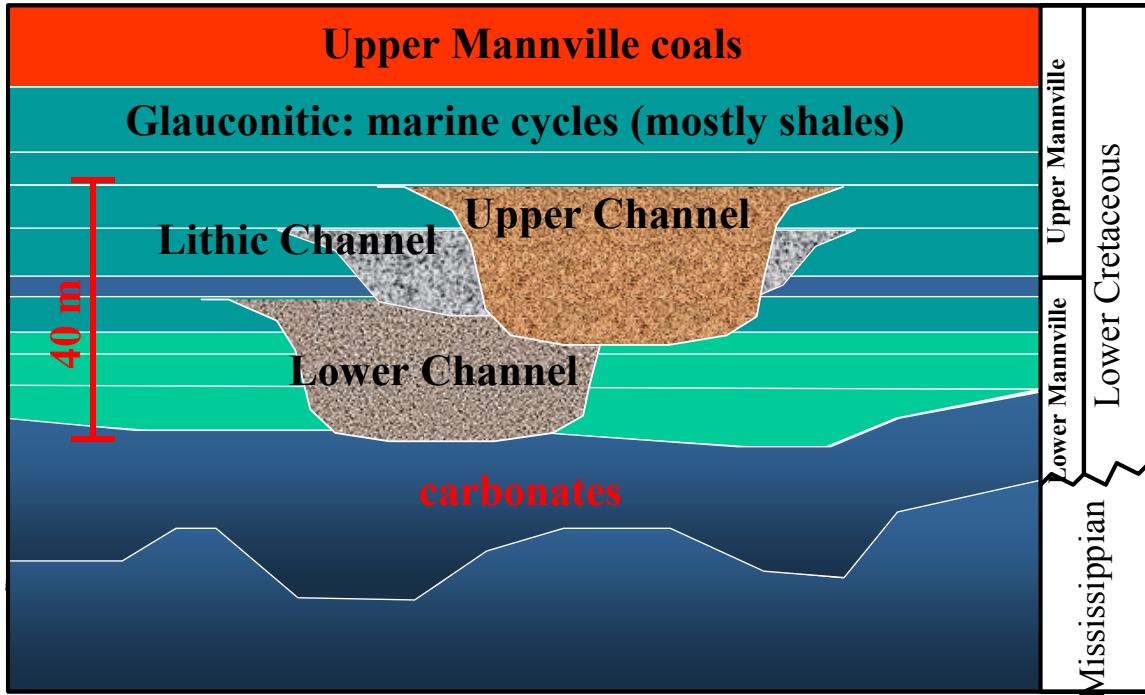
Figure 1. The Glauconitic channel system at Blackfoot oil field, Alberta, is a sequence of sand and shale filled valleys incised into Lower Cretaceous and Mississippian carbonates. The Blackfoot interpretation has an upper and lower channel that are prospective and separated by a non-porous lithic channel.
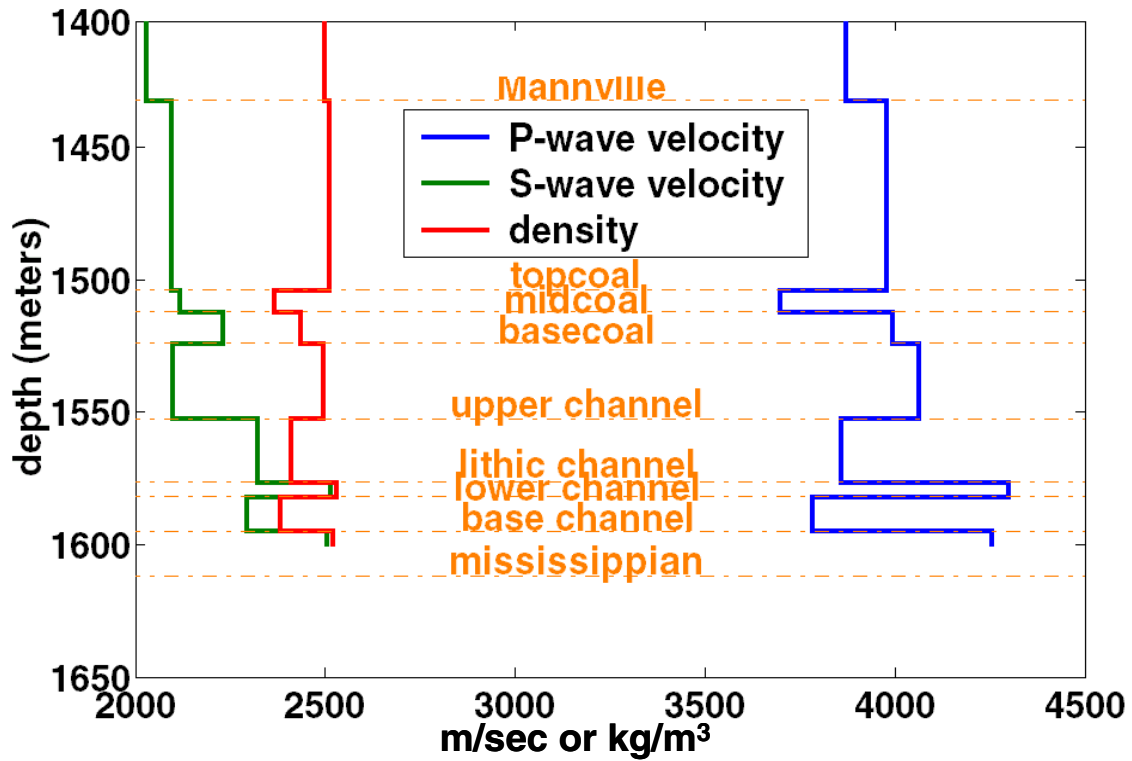
Figure 2. Blocked well logs for a producing oil well at Blackfoot field. At the top of the upper channel, density and P-wave velocity decrease while S-wave velocity increases. At the base of the lower channel, all logs show an increase.
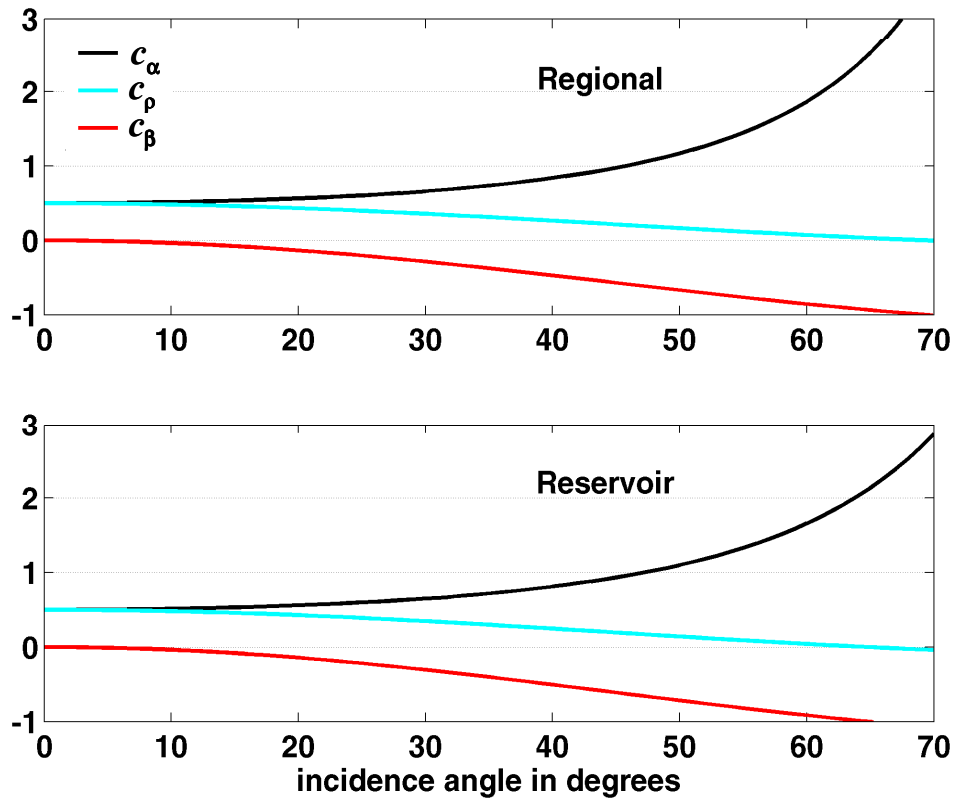
Figure 3. The coefficients $c_\alpha, c_\rho, c_\beta$ of the Aki and Richards approximation $R_{pp} \approx c_\alpha f_\alpha + c_\rho f_\rho + c_\beta f_\beta$ are shown as a function of the incidence angle. The elastic parameters are defined in Table 1.
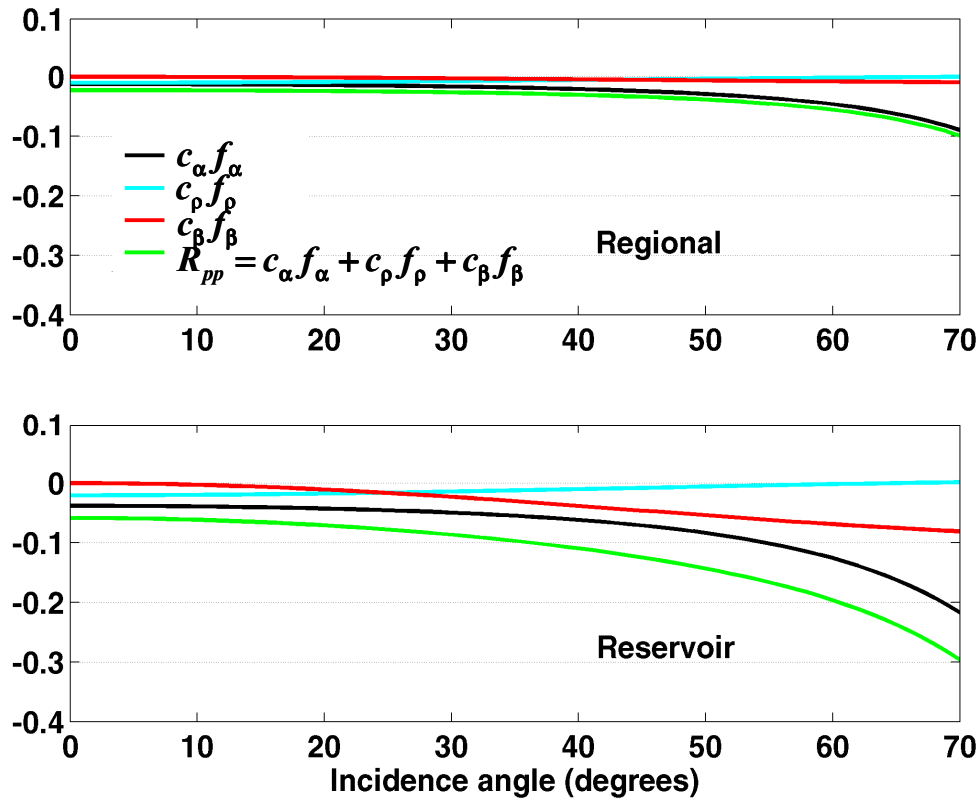
Figure 4. Using the values for the fluctuations $f_\alpha, f_\rho, f_\beta$ from Table 1 and the coefficients $c_\alpha, c_\rho, c_\beta$ from Figure 3, the partial reflection coefficients for P-wave velocity, $c_\alpha f_\alpha$, density, $c_\rho f_\rho$, and S-wave velocity, $c_\beta f_\beta$ may be computed. Also shown is the total reflection coefficient $R_{pp} = c_\alpha f_\alpha + c_\rho f_\rho + c_\beta f_\beta$.
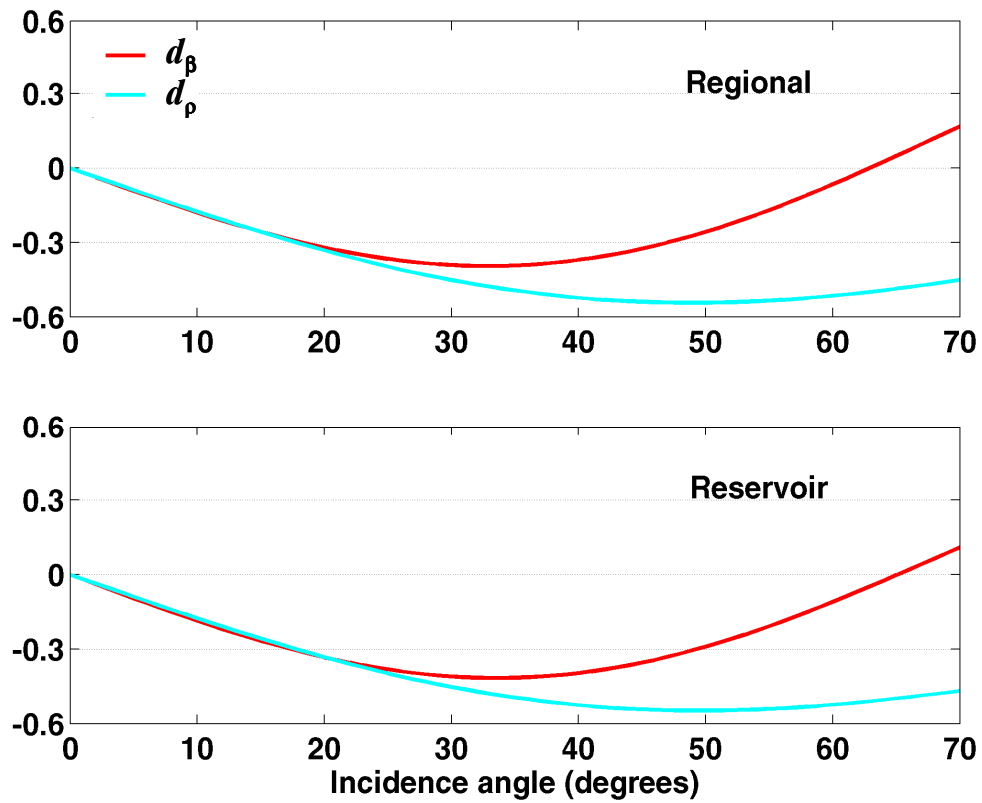
Figure 5. The coefficients d_β, d_ρ of the Aki and Richards approximation $R_{ps} \approx d_\beta f_\beta + d_\rho f_\rho$ are shown versus P-wave incidence angle. The elastic parameters are as given in Table 1.
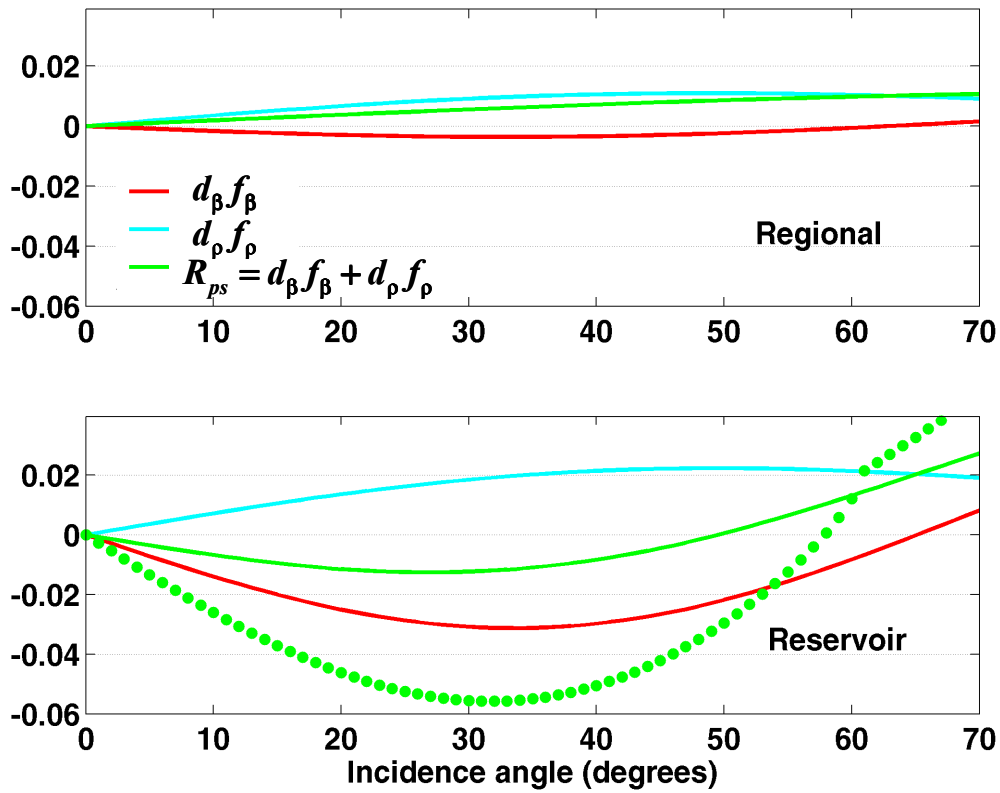
Figure 6. The product of the fluctuations f_β, f_ρ from Table 1 with the curves of Figure 5 allows the calculation of the contributions to R_{ps}. The S-wave term $d_\beta f_\beta$ (red) and the density term $d_\rho f_\rho$ combine to give the total R_{ps} (green). The difference in sign between $d_\beta f_\beta$ and $d_\rho f_\rho$ results in a small R_{ps}. If $d_\beta f_\beta$ were positive, the result would be the green dots.
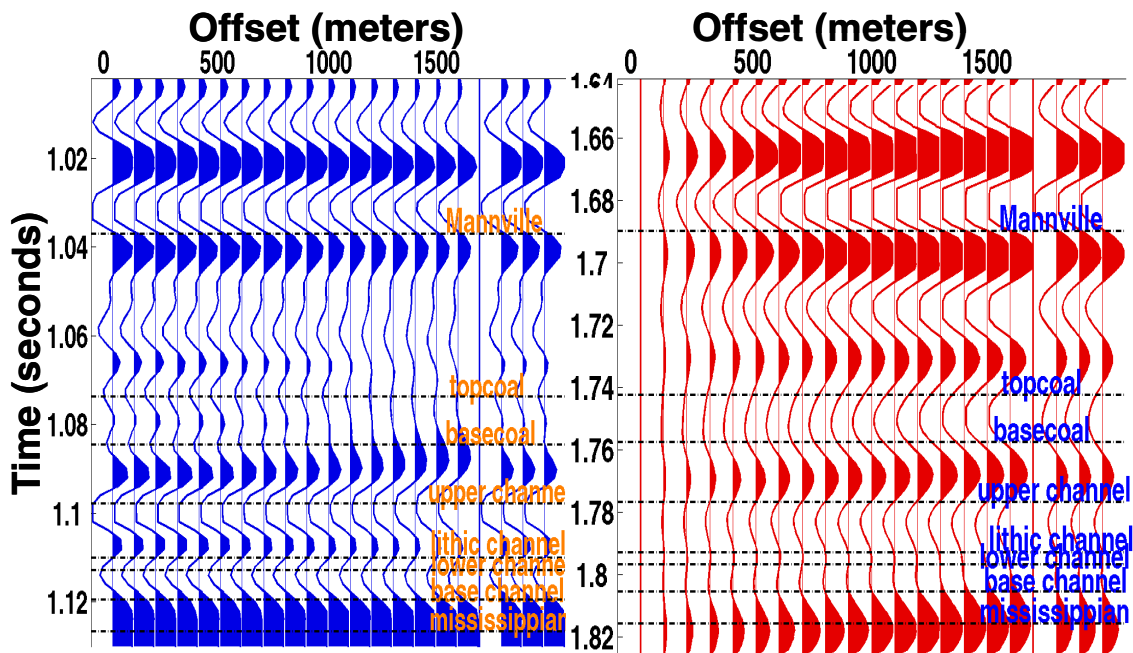
Figure 7. P-P (blue) and P-S (red) synthetic seismograms for the well logs of Figure 2. (The seismograms were made from the unblocked logs.) In each seismogram, the three traces on the right are three repetitions of the stacked trace. The P-P seismogram has a 10-80 Hz zero-phase wavelet while the P-S seismogram has a 10-40 Hz zero-phase wavelet. Despite this difference in bandwidth, the seismograms show similar resolution.

Limited-offset volumes
P-P CMP stacks

0-450m   225-675m   450-900m   675-1135m   900-1350m

P-S depth variant CCP stack

0-700m   350-1050m   700-1400m   1050-1750m   1400-2100m
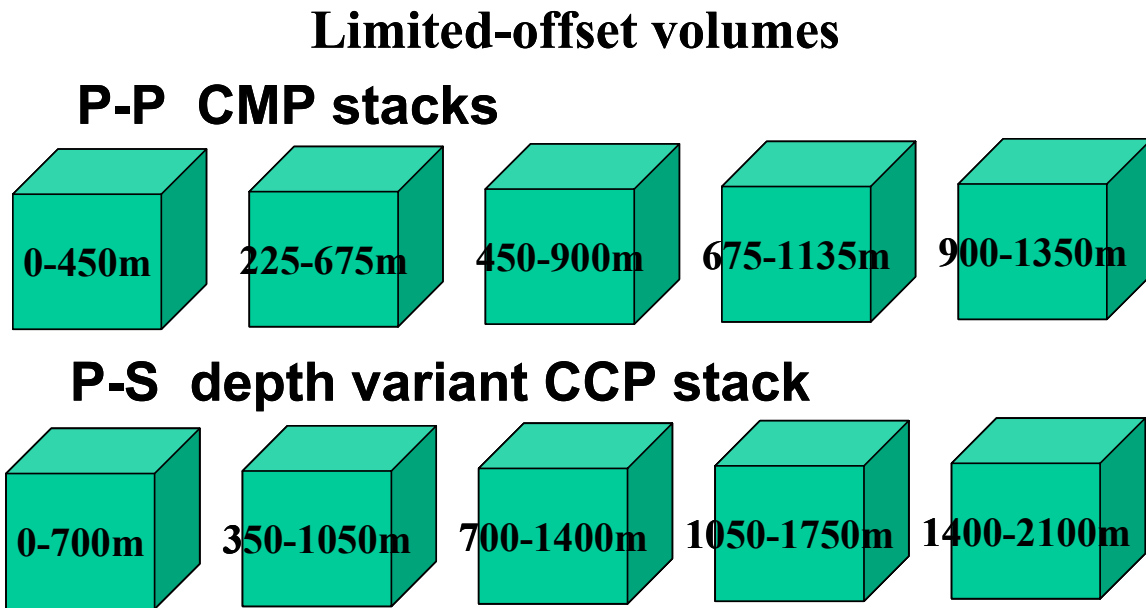
Figure 8. The Blackfoot 3C-3D data were taken through appropriate P-P and P-S processing flows and then stacked into limited offset volumes.

Each cube

TVSW → Fxy Pred. → Migration → Flatten → Amplitude restoration → Horizon slices
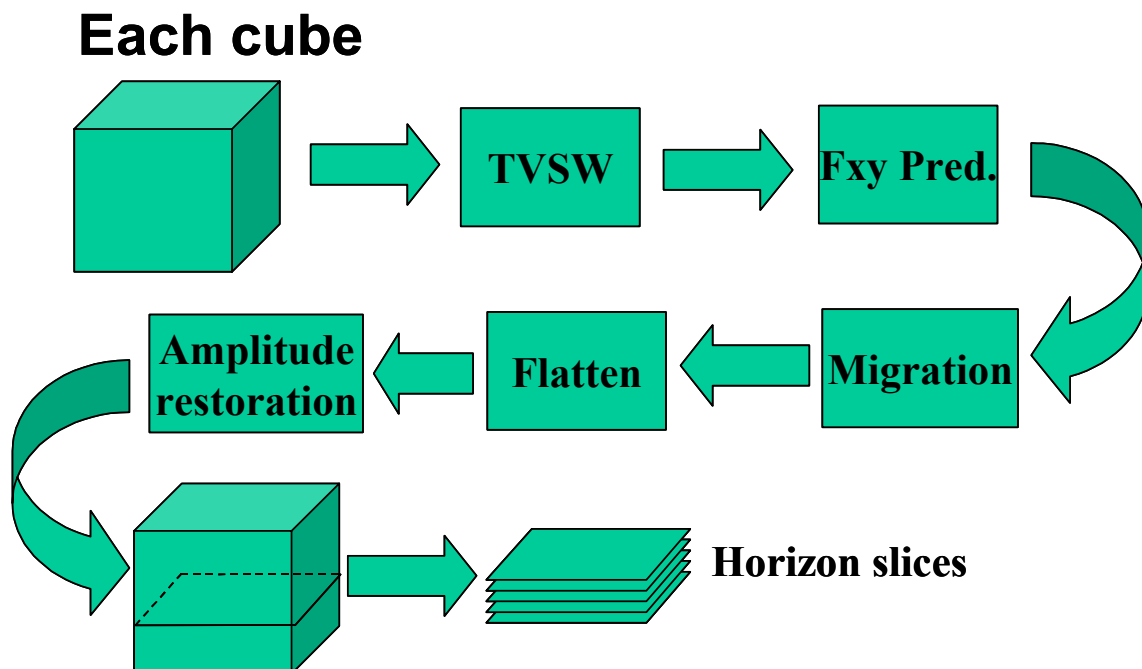
Figure 9. Each limited offset 3D volume of Figure 8 was taken through a post stack process of event enhancement, migration, flattening on a reference event just above the channel, amplitude

restoration, and finally horizon slicing. The horizon slicing was preceded by a conversion to depth relative to the reference event.

P-P slices

P-S slices

$$\frac{\Delta I}{I}, \frac{\Delta J}{J}, \ldots$$
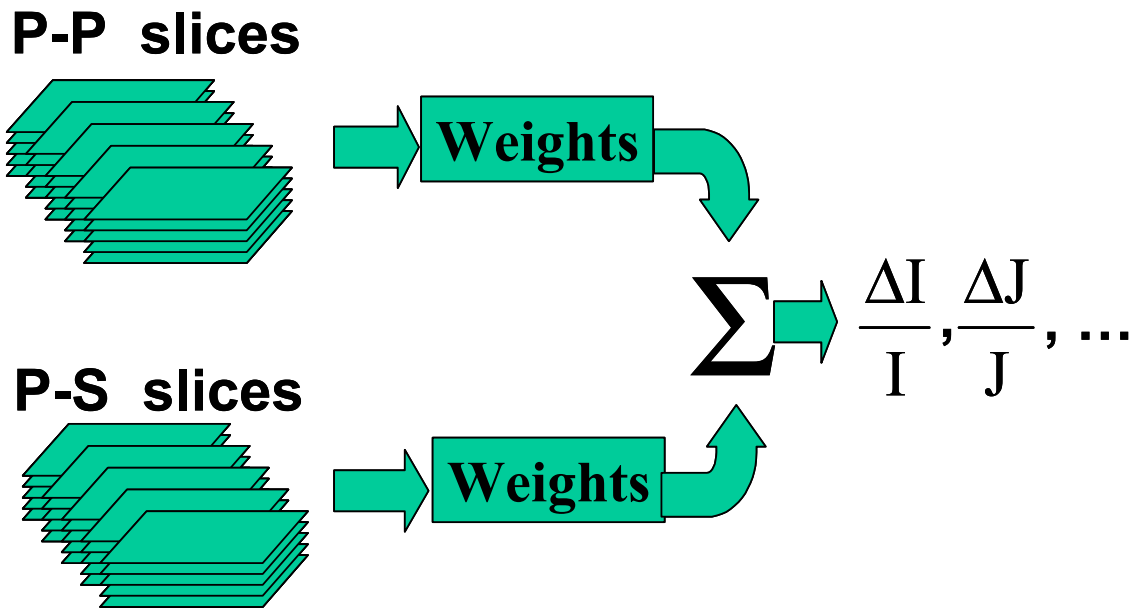
Figure 10. P-P and P-S simultaneous weighted stacking. After the processes of Figures 8 and 9, ten sets of offset-binned horizon slices were available. Since these data were converted to depth relative to a reference horizon just above the channel, they are effectively P-P and P-S reflection coefficient estimates at equivalent stratigraphic levels. Impedance reflectivity estimates were created by weighting the horizon slices and stacking as described in the text. At each stratigraphic level, ten weighted horizon slices were combined to create each impedance fluctuation estimate.
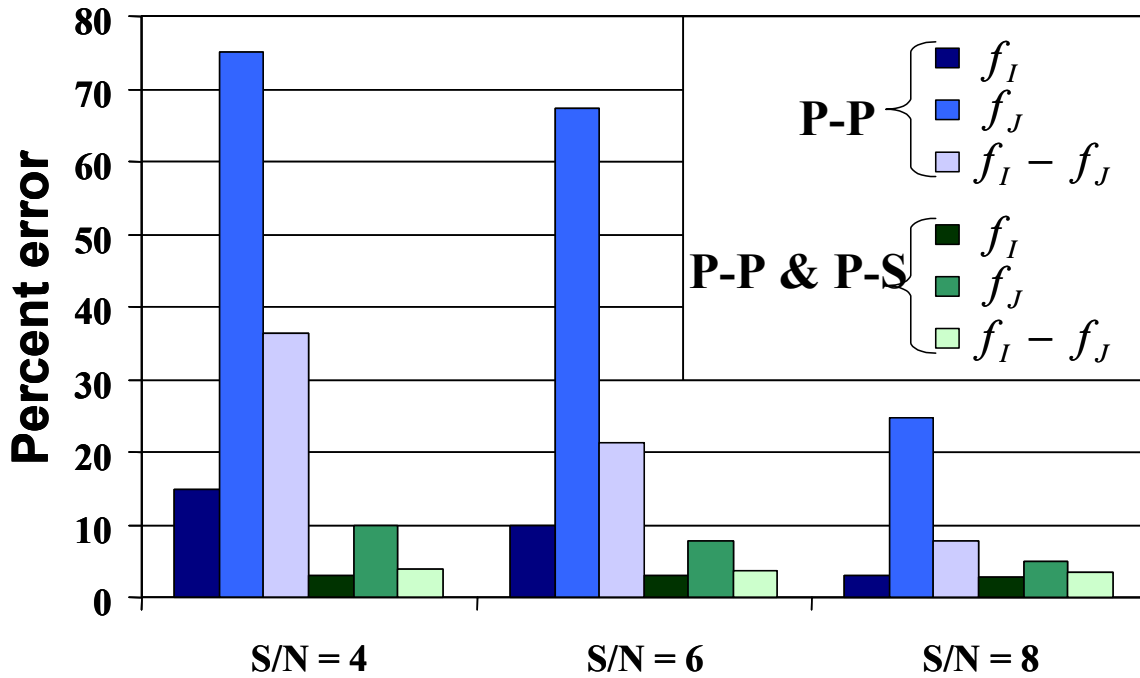
Figure 11. The results of a comparison of the P-P inversion and the simultaneous P-P and P-S inversion for a simple synthetic consisting of a single reflector with reflection amplitudes taken from the exact Zoeppritz equations. Percent error is shown for three different signal-to-noise (S/N) ratios. The advantages of the simultaneous method increase as S/N decreases.
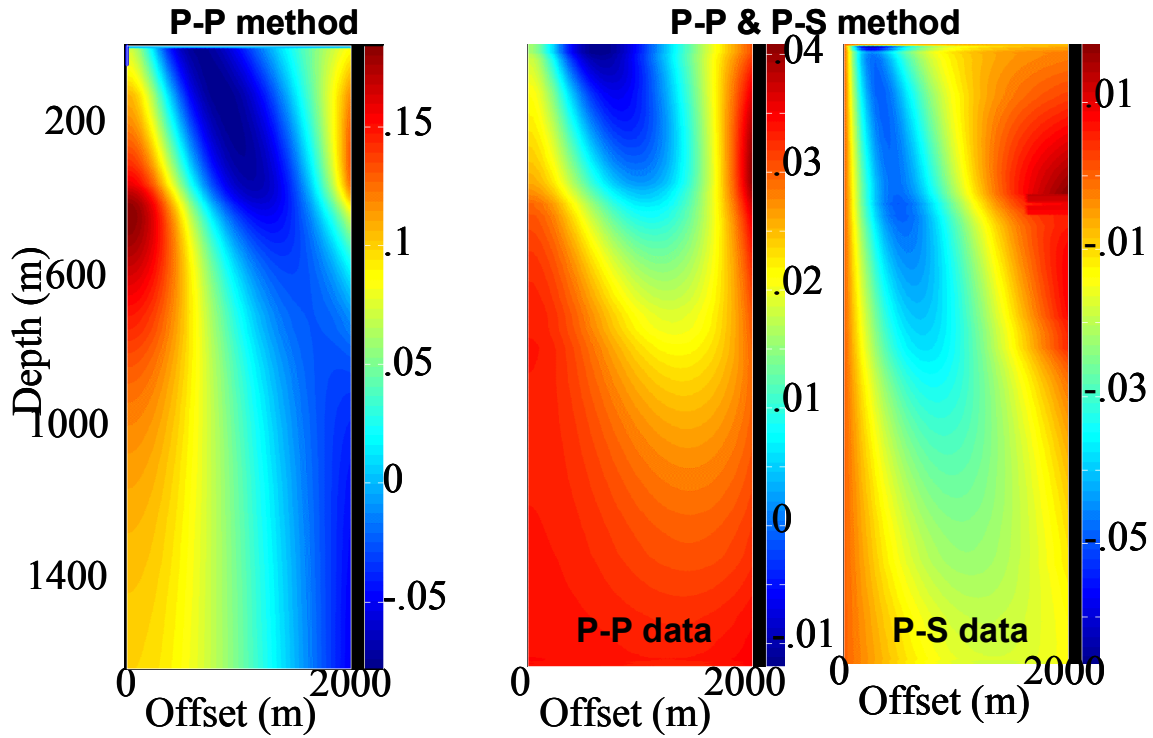
Figure 12. The stacking weights required to estimate $f_I = \Delta(\rho\alpha)/(\rho\alpha)$ are shown for the P-P method (left) and the P-P & P-S simultaneous method (right). The simultaneous method requires two sets of weights, for both P-P and P-S data. The P-P method tends to subtract far from near offsets while the simultaneous method tends to subtract the two different datasets.
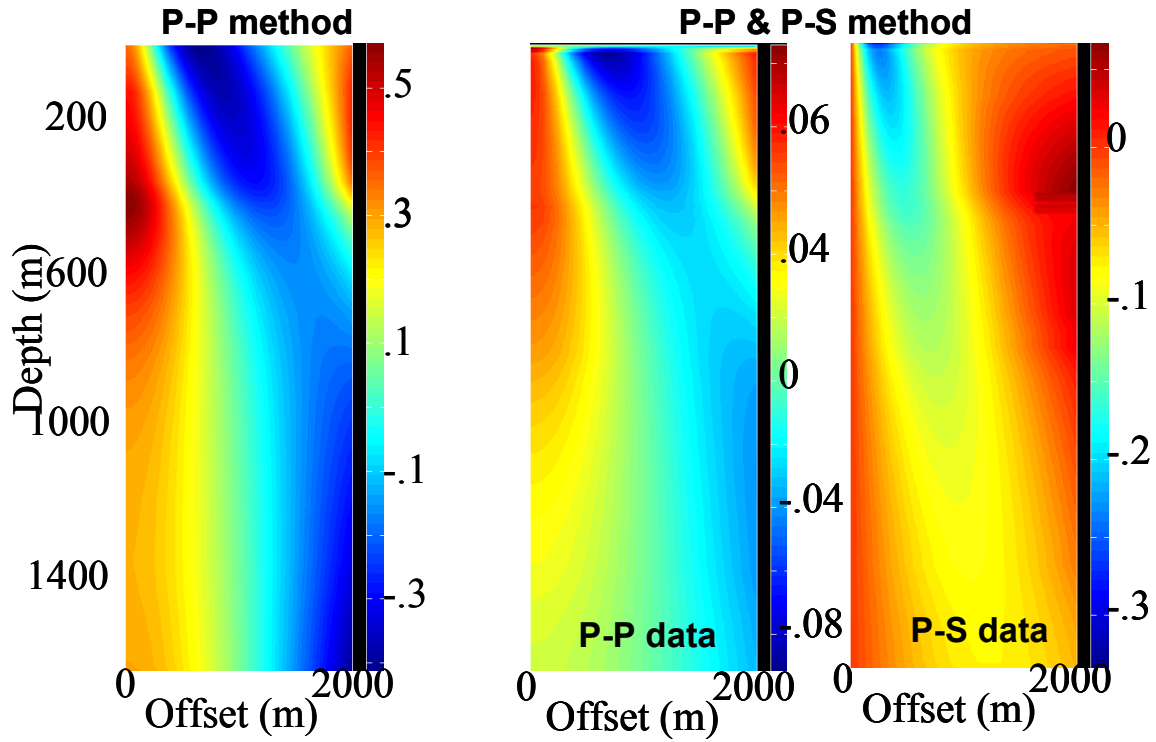
Figure 13. The stacking (least squares inversion) weights required to estimate $f_J = \Delta(\rho\beta)/(\rho\beta)$ are shown for the P-P method (left) and the P-P & P-S simultaneous method (right). The P-P method strongly subtracts far from near offsets while the simultaneous method emphasizes the P-S data.
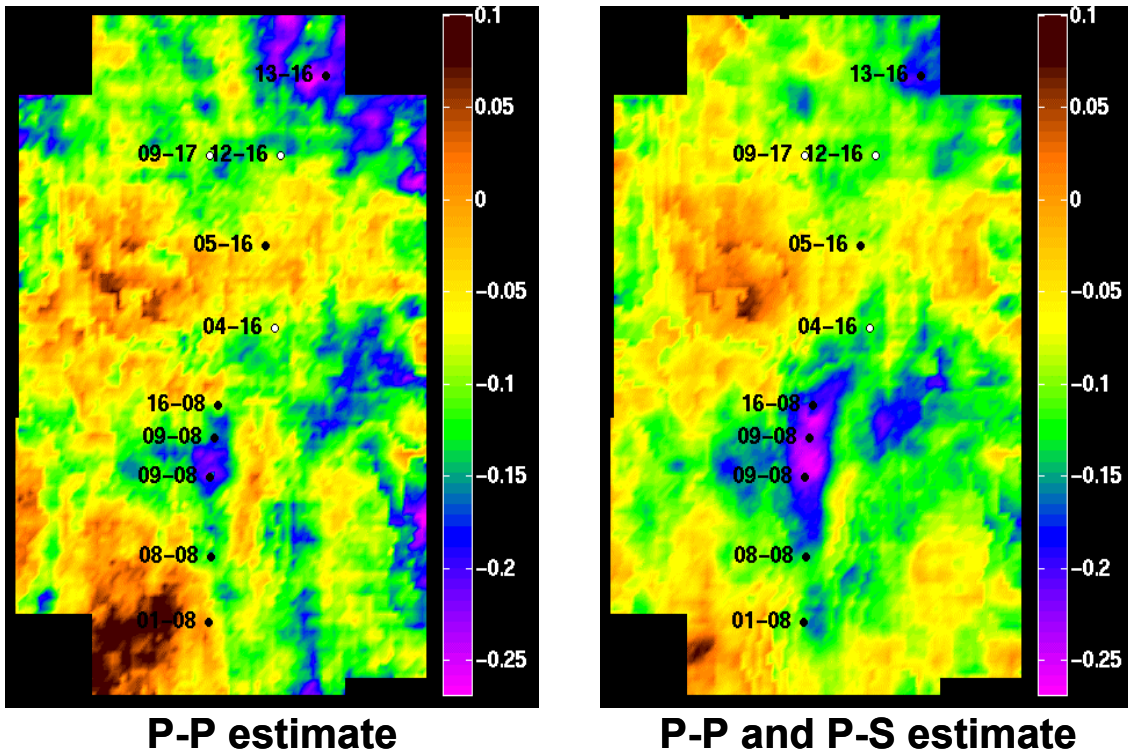
Figure 14. Fluctuation of compressional impedance, top of upper channel as estimated from P-P data alone (left) and P-P simultaneously with P-S data (right). The black circles are producing wells and the white circles are dry holes. The producing channel runs south-north in the lower center of the Figure as identified by the trend of producing wells.
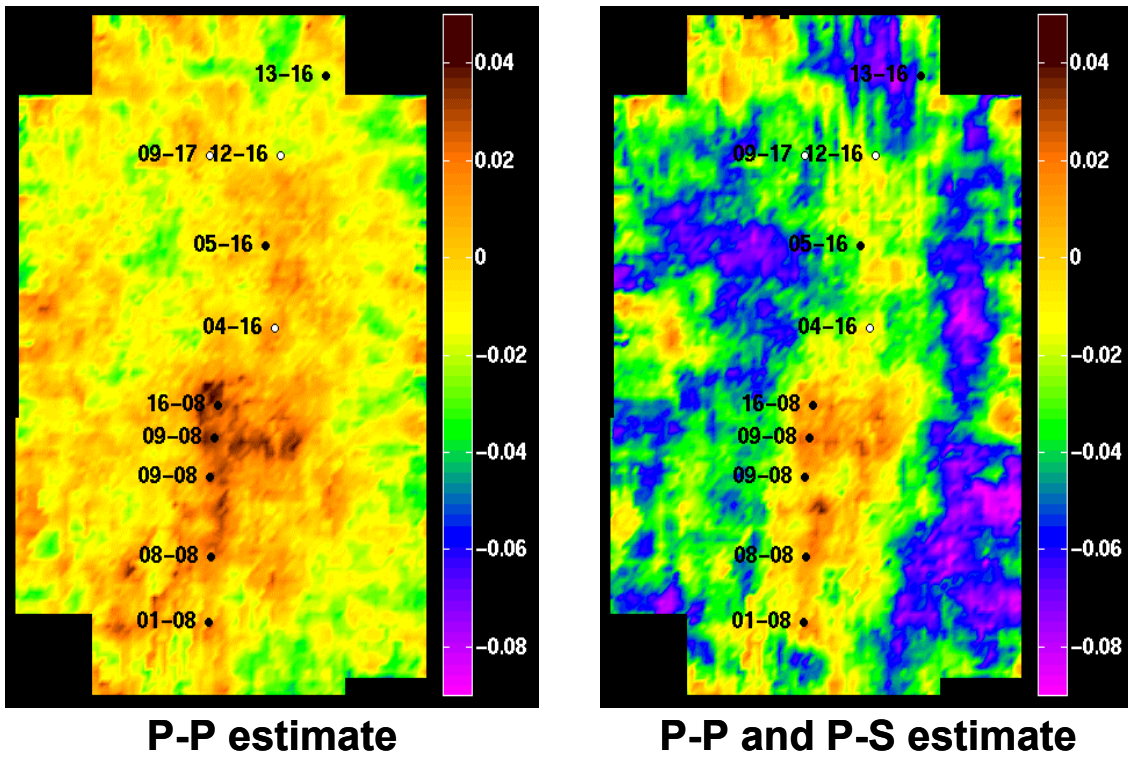
P-P estimate   **P-P and P-S estimate**

Figure 15. Fluctuation of shear impedance, top of upper channel, as estimated from P-P data (left) and both P-P and P-S data (right). See Figure 14 for further discussion.
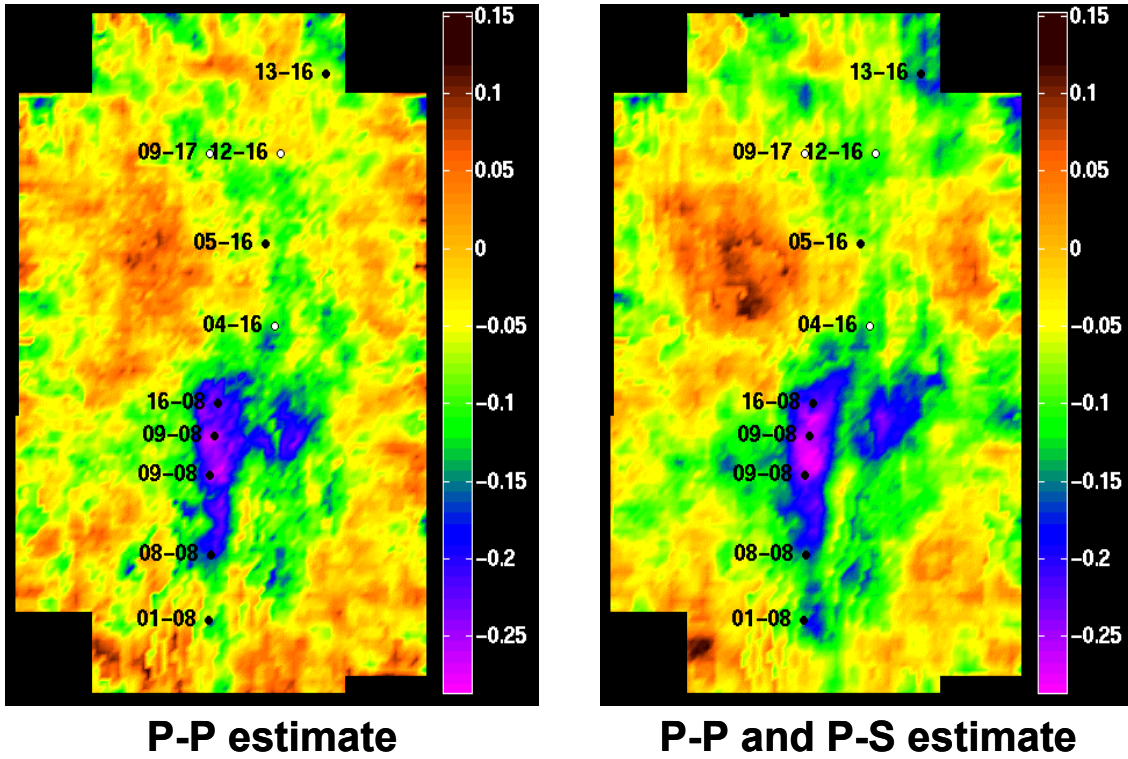
Figure 16.   Pseudo-Poisson's ratio fluctuation at top of upper channel, as estimated from P-P data (left) and both P-P and P-S data (right).   This is just the subtraction of the map of Figure 15 from that of Figure 14.   See Figure 14 for further discussion.

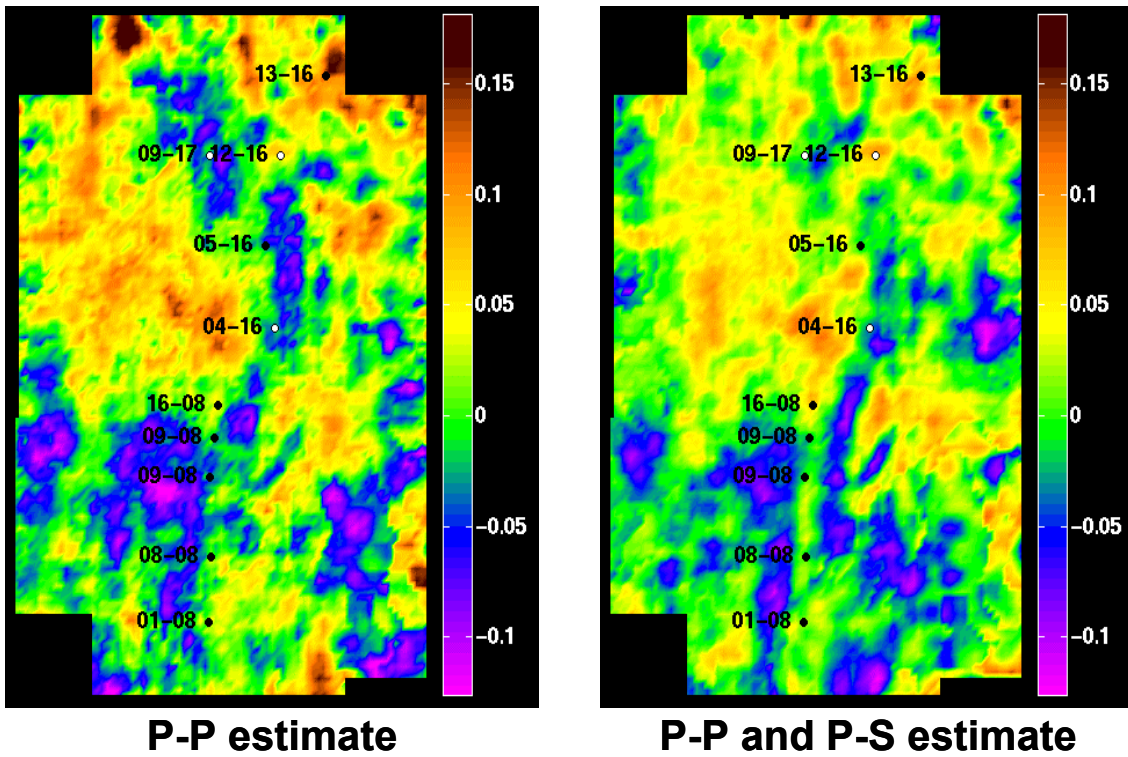**P-P estimate**   **P-P and P-S estimate**

Figure 17. Fluctuation of compressional impedance, bottom of lower channel, as estimated from P-P data alone (left) and P-P simultaneously with P-S data (right). The vertical trend of producing wells (black circles) in the lower center of each image identifies the channel system.

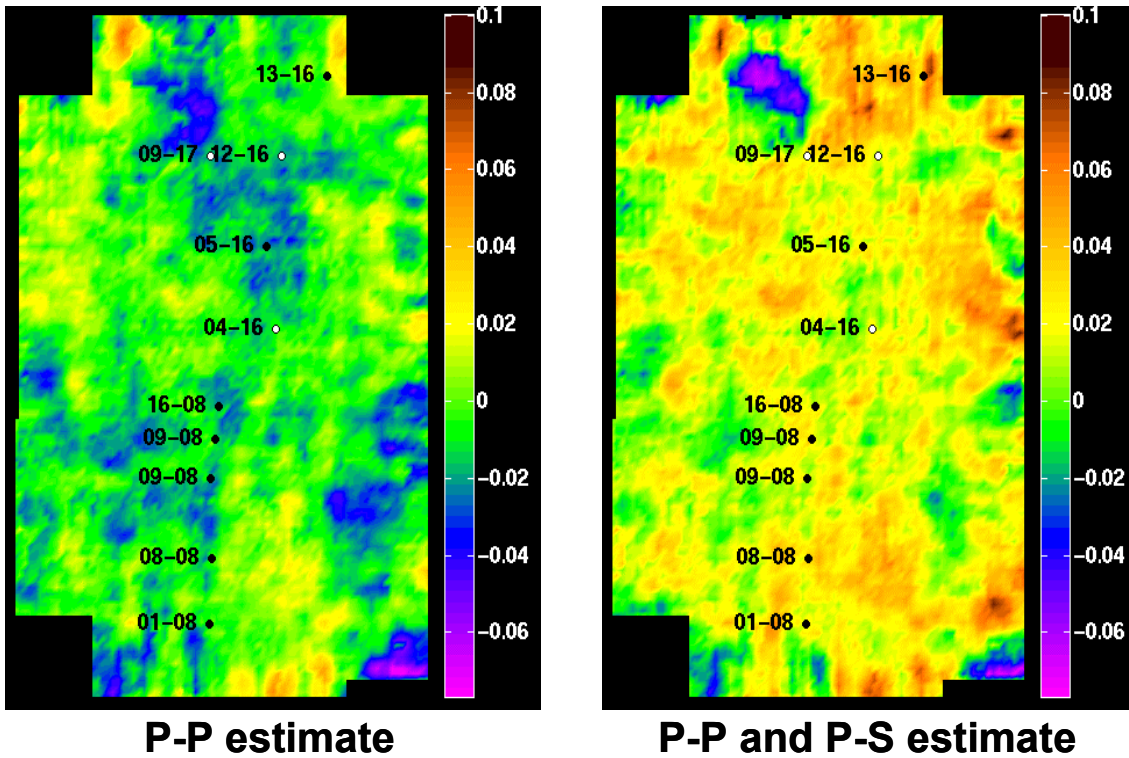**P-P estimate**   **P-P and P-S estimate**

Figure 18. Fluctuation of shear impedance, bottom of lower channel, as estimated from P-P data alone (left) and P-P simultaneously with P-S data (right). The vertical trend of producing wells (black circles) in the lower center of each image identifies the channel system.
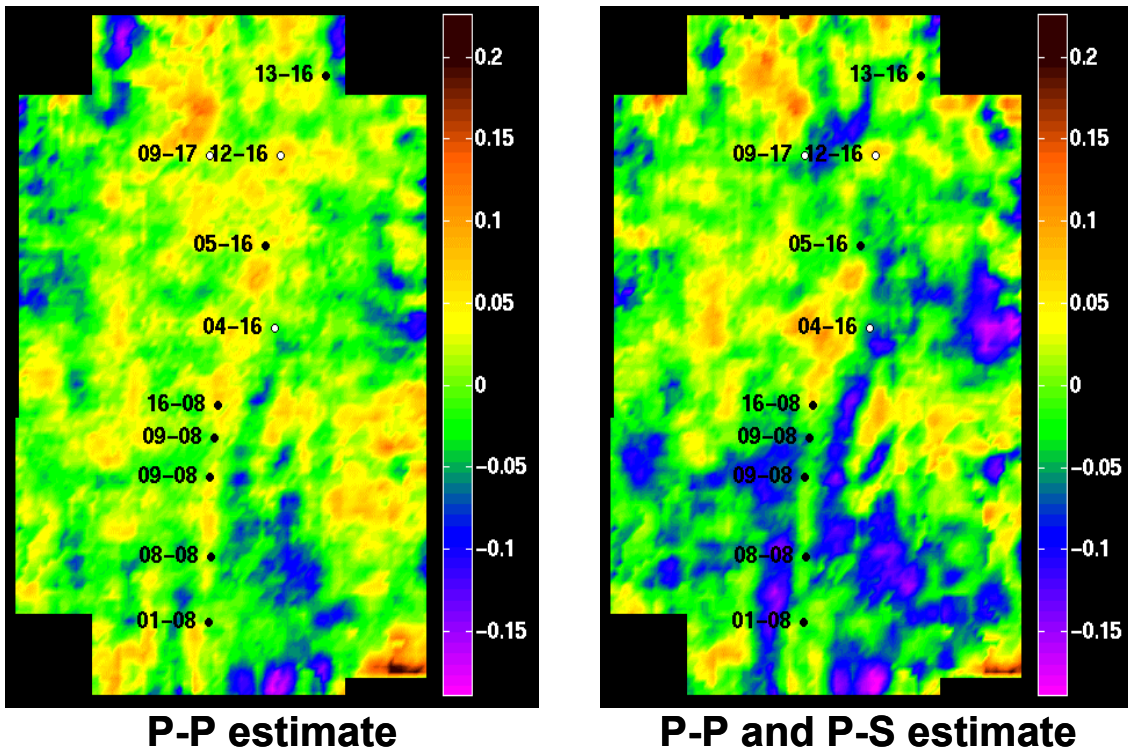
P-P estimate   **P-P and P-S estimate**

Figure 19. Pseudo-Poisson's ratio fluctuation, bottom of lower channel, as estimated from P-P data alone (left) and using both P-P and P-S data (right). Note the target channel as indicated by the producing wells (black circles) trending vertically in the lower center of each image.